GEO4-1442: Modelling crust & lithosphere deformation numerical modelling of continental extension

C. Thieulot & L. Jeanniot

October 2017

Contents

1 Geological Context **2**
1.1 Conceptual models . . . 2
1.2 Analogue models . . . 2
1.3 Numerical models . . . 2

2 Methodology **4**

3 Effect of plastic-viscous layering and strain softening on mode selection during lithospheric extension **6**
3.1 Let's run the code . . . 7
3.1.1 Using Paraview . . . 7
3.1.2 Using gnuplot . . . 9
3.2 Tasks ahead . . . 10
3.3 Effect of lower layer viscosity - model1 . . . 10
3.4 A first look at temperature - model2 . . . 11
3.5 Temperature-dependent density - model3 . . . 11
3.6 Temperature-dependent density and viscosity - model 4,5 . . . 11
3.7 Temperature-dependent density and viscosity with diffuse seed - model 6 . . . 11
3.8 Food for thought and bonus questions . . . 12

Please do not print this document. It will most likely be altered/improved upon in class.

1 Geological Context

The formation of a new ocean during plate tectonics requires stretching, thinning and breakup of a continental plate into two or more fragments. The deformation of the lithosphere during continental rifting leads to mantle upwelling, which at some point generates melt by mantle decompression creating a new oceanic crust. The investigation of the crust and lithosphere deformation during continental rifting is possible via geological and geophysical observations, and by using different model approaches.

Understanding extensional processes on the real Earth primarily and indubitably relies on the studies of past or currently-active regions under extension. Those regions includes any simple sedimentary basins, active or aborted rift systems, present-day continental rifted margins or fossil analogues margins exposed in orogens. The types of observations are diverse including field-geology observations, seismic imaging, tomography and much more. All those data require interpretation and explanation which lead to new concepts and generation of models.

1.1 Conceptual models

Conceptual models are more or less elaborate cartoons based on geological and geophysical observations. They help to visualize concepts in a simple manner and they can be considered as the first step in understanding lithosphere deformation. For example, the concept of pure shear ([23]) and simple shear ([28]), as shown in Fig. (1) are two important contributions to explain associated rift and margin geometries during lithosphere extension. [12]

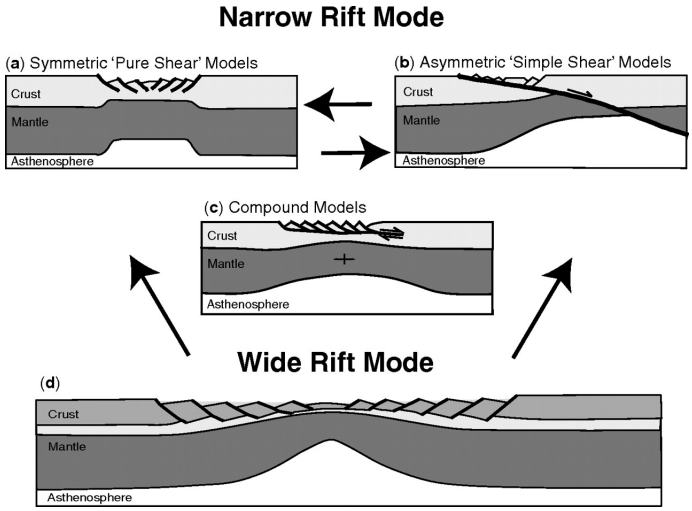

Figure 1: End-member styles of rifting; symmetric, asymmetric and compound ([22]) narrow models, and the wide rift mode. (from [15])

1.2 Analogue models

Analogue modelling is performed in laboratories and uses different types of materials to reproduce and simulate features of crustal and lithosphere deformation (see for instance Fig. (2)). While analogue models are simple, intuitive and good for 3D, they cannot take into account a complicated rheological evolution.

1.3 Numerical models

Numerical modelling is a necessary tool for geodynamics since tectonic processes are too slow and too deep in the Earth to be observed directly. Since the 1980s, numerical geodynamic modelling has been developing very rapidly in terms of both the number of various applications and numerical techniques explored. Many geodynamic problems can be described by mathematical models, i.e. by a set of partial differential equations and boundary and/or initial conditions defined in a specific domain. Numerical models are based on the general physical-mechanical principles (e.g., momentum, thermal, and mass conservation equations) and predict what would happen when the crust and mantle deform slowly over geological time. The equations involved can be solved with a specific numerical method (e.g., Finite Difference Method, Finite Element Method, etc).

When looking at a specific geological problem, one first needs to design an initial model with certain boundary conditions. Then the model can be simulated by running a computer code, which produces the time-dependent evolution of the model.

Two types of numerical modelling approaches can be discriminated: kinematic and dynamic approaches.

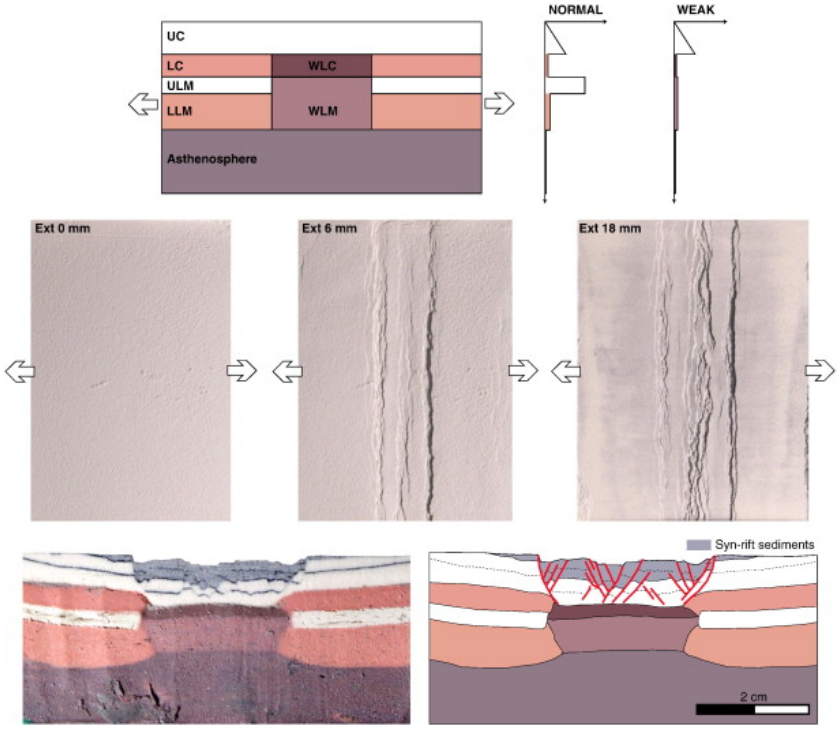

Figure 2: Evolution of a 4-layer experiment containing 3-layer weakness zone for comparison with the East African Rift System. (from [10])

In kinematic models, the crust and lithosphere deformation is prescribed by a flow velocity field. The flow field can be an analytical solution (e.g., pure shear deformation mode of [23]), or coming from a numerical solution [18]. This allows the advection of temperature and material and thereby the total control of the resulting deformation. Although kinematic models omit rheological properties and the physics of its evolution, their simplicity of use allows quantitative calibration on natural case laboratories. Kinematic models can be applied to predict e.g., subsidence, heat-flow or the architecture of sedimentary basins and rifted margins. In [18], a kinematic model was developed to determine the full deformation history of the Iberia-Newfoundland rifted margins formation (Fig. 3).

In dynamic models as shown in Fig. (4), the mode of lithosphere deformation is defined by constitutive equations where the rheology is fully thermo-mechanically coupled ([25]), and thus often showcases nonlinear couplings: heat transport (e.g. thermal convection), phase changes, complex rheology (e.g. non-Newtonian flow, strain softening, elasticity and plasticity - [14, 17, 15]), melting and melt migration ([6, 20]), chemical reactions, solid body motion, lateral forces, etc.

Lithosphere and asthenosphere deformation is usually initiated using initial anomalies implanted within the lithosphere[1] (e.g., difference in crustal thickness, weak viscosity seed [26, 11]). These models show a complex evolution determined by the initial limit conditions and rheological properties of the continental crust and mantle, but they may result in unexpected predictions, which make them difficult to apply to specific rifted margins architecture and calibrated against real data observations.

Applications of numerical dynamic models to continental rifting processes are varied and numerous. To give a few examples, the mode of extension and margin architecture can be examined by introducing depth-dependent extension [16, 13], rheological layering in the crust [29] or in the mantle [21], salt [1, 2], erosion [9], etc, in order to analyze processes such as rift propagation [27] or extensional features such as rifted margin architecture [30] or sedimentary basin styles [8]. In addition, numerical models are very handy for 3D modelling [3, 4, 5], and can even be compared to analogue model results [7].

Very recently Naliboff and co-workers have demonstrated, in unprecedented detail, how faults formed in the earliest phases of continental extension control the subsequent structural evolution and complex architecture of rifted margins through fault interaction processes, hereby creating the widely observed distinct margin domains, see Fig(5).

[1] http://blogs.egu.eu/divisions/gd/2017/10/18/planting-seeds-of-deformation-in-numerical-models/

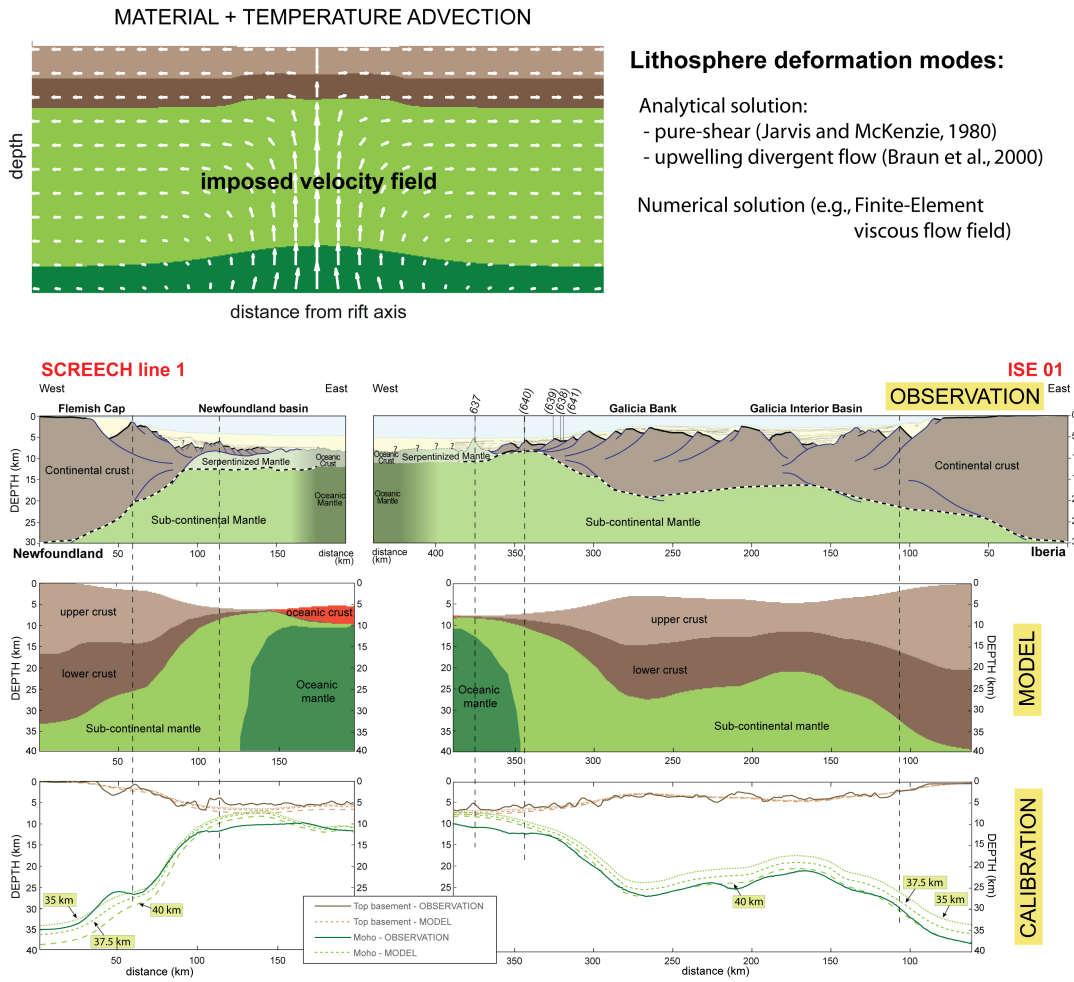

Figure 3: Application of a kinematic model of lithosphere deformation to the Iberia-Newfoundland rifted margins formation (from [18])

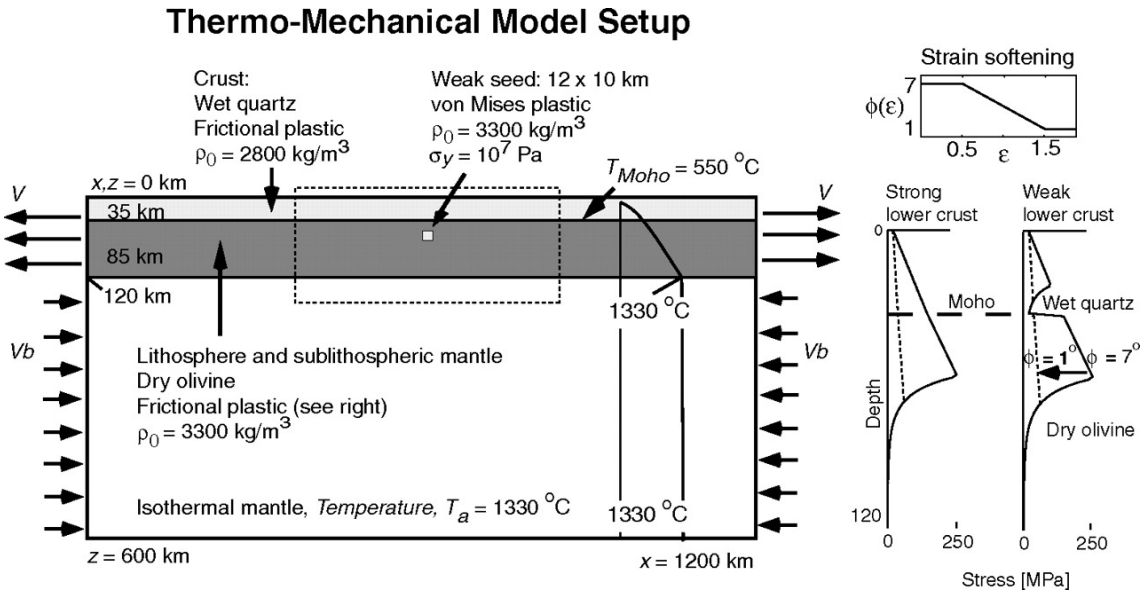

Figure 4: Example of a dynamic model setup ([14])

2 Methodology

We will use the state-of-the-art geodynamical code ELEFANT, a thermo-mechanically coupled Finite Element code [25]. It solves the incompressible flow Stokes equations (mass and momentum conservation equations) as well as the

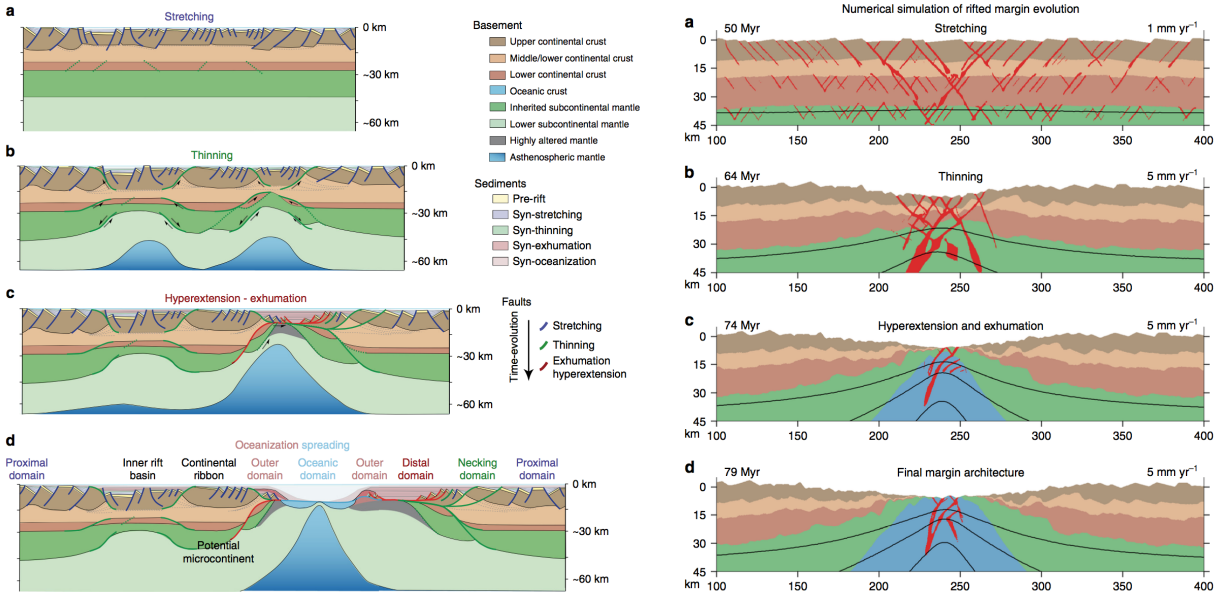

Figure 5: Figures taken from [24]. Left: Schematic model of the phases of rifted margin formation. Right: Modeled phases of rifted margin formation.

heat transport equation:

$$-\boldsymbol{\nabla} p + \boldsymbol{\nabla} \cdot (2\mu(\dot{\boldsymbol{\epsilon}}, p, T)\dot{\boldsymbol{\epsilon}}) = \rho(T)\boldsymbol{g} \quad (1)$$

$$\boldsymbol{\nabla} \cdot \boldsymbol{v} = 0 \quad (2)$$

$$\rho c_p \left(\frac{\partial T}{\partial t} + \boldsymbol{v} \cdot \boldsymbol{\nabla} T \right) = k\Delta T + H \quad (3)$$

where p is the pressure, $\dot{\boldsymbol{\epsilon}}$ is the strainrate tensor, μ is the dynamic viscosity, $\rho(T)$ is the mass density, $\boldsymbol{g}$ is the gravitational acceleration, T is the temperature, $\boldsymbol{v}$ is the velocity, c_p the heat capacity coefficient, k the heat conductivity coefficient, and H is a source term.

It is well known that the viscosity of Earth materials depend on temperature, pressure, strainrate and potentially other quantities which are not tracked here (e.g. melt content). This renders Eq.(1) nonlinear, i.e. one of the coefficients of the PDE depends on the solution of this PDE.

In what follows we will restrict ourselves to two-dimensional calculations in the (x, z) plane. The code discretises the coupled set of PDEs on a computational grid of size $L_x \times L_z$ counting $ncell = ncellx \times ncellz$ cells/elements, as shown on the following figure:

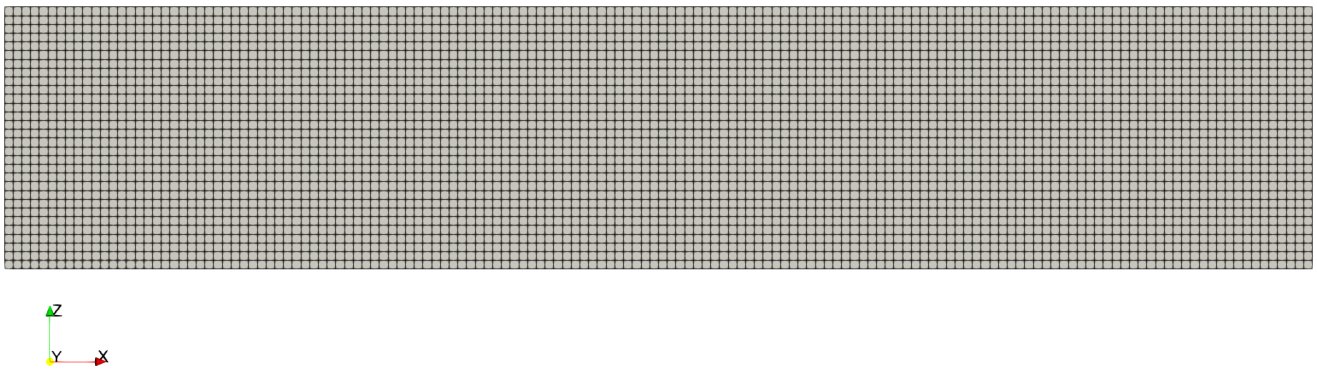

The grid points constituting the top row of the grid define the discrete free surface of the domain. Once the Eulerian velocity field has been computed on these, their position is first updated using a simple Eulerian advection step.

The following figure shows the computational mesh after a few kilometers of extension:

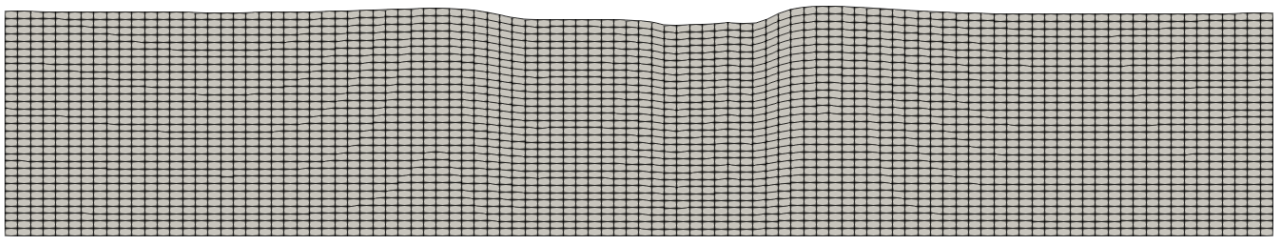

Note that the length of the grid remains constant throughout the simulation so that there actually is an outward flux of material through the left and right boundaries. This technique is called Arbitrary Lagrangian Eulerian and is described in [25].

The code alternatively solves the mass+momentum conservations equations and the heat transport equations. The latter equation contains a (partial) time derivative and time-stepping is then necessary. Discrete time steps are then taken: a 'snapshot' of the system (i.e. PDEs are solved) is computed at regular intervals δt in time until the simulation total time t_{final} is reached.

Materials are tracked throughout the simulation by means of so-called Lagrangian markers. Each marker tracks a type of material. The movement of the markers tracks the flow of the materials present in the simulation. They are needed since the grid does not deform with the computed velocity.

At the beginning of the simulation a given number of markers is random placed inside each element. Each is assigned a material, and the swarm of markers is painted with a checkerboard pattern which will allow for (visual) deformation tracking, as shown on the following figure:

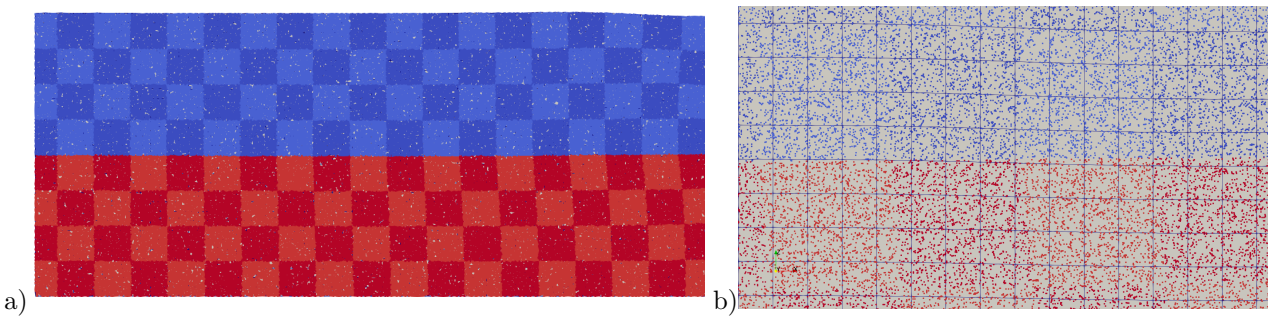

a) example of checkerboard paint on a marker swarm; b) zoom in on a few elements

Markers also record the accumulated strain, which can feed back into the rheology, as explained in the next section.

3 Effect of plastic-viscous layering and strain softening on mode selection during lithospheric extension

This experiment is based on Huismans et al. [17]. in which the authors look at the factors controlling the selection of deformation modes during continental extension using analytical and numerical methods. They view the lithosphere as a laminate and examine a simple system with a uniform plastic layer overlying a uniform linear viscous layer. The rate of energy dissipation is analyzed for pure shear (PS), symmetric plug (SP), and asymmetric plug (AP) extension modes.

More precisely, we will be focusing on reproducing and exploring further the results presented in Fig. (6) of this paper. In that case only the cohesion of the plastic layer can undergo strain-weakening since the angle of friction ϕ is set to zero. In the code, strain is tracked and accumulated in the domain on the markers. It feeds back into the rheology as shown hereunder. For strain values $\epsilon < \epsilon_1$ the cohesion remains constant at c. For strain values $\epsilon_1 < \epsilon < \epsilon_2$ the effective cohesion decreases linearly, and for $\epsilon > \epsilon_2$ it remains constant at c^{sw}.

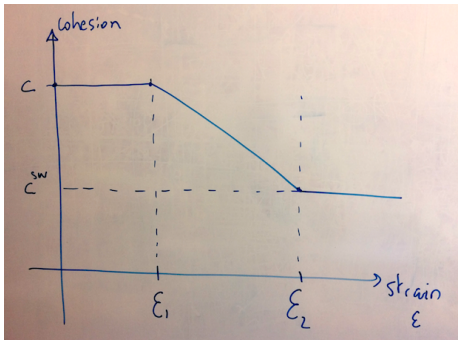

Extension is seeded by a small plastic weak seed placed at the base of the plastic layer. This seed contains the same material as the top layer but its cohesion has been set to c^{sw}.

The model has a free top surface, and the other boundaries have zero tangential stress (free slip). Sedimentation and erosion are not included in the model. Horizontal extensional velocities ($\pm V_{ext}$) are imposed on each side of the domain.

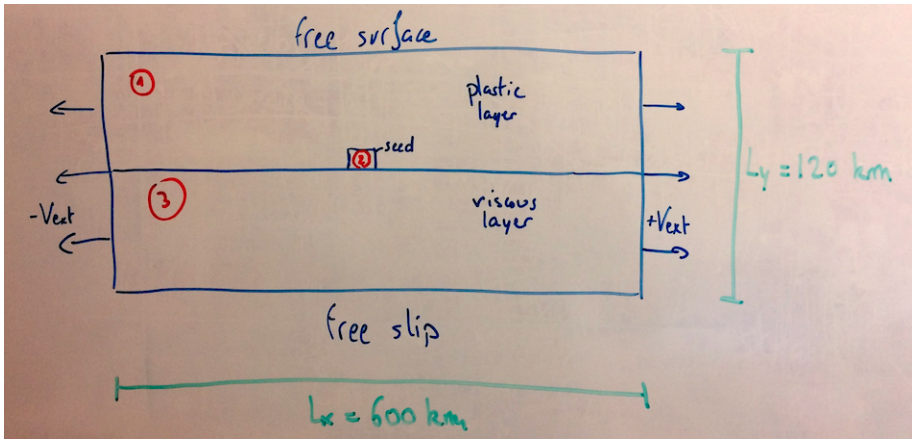

Values and units of all relevant parameters are given in the following table:

Symbol	Meaning	Value
L_x	domain size in x direction	600km
L_z	domain size in z direction	120km
c	cohesion	230MPa
c^{sw}	strain-weakened cohesion	30 MPa
μ_0	viscosity	$10^{21-22-23}$ Pa.s
V_{ext}	extension velocity	1cm/yr
ρ_0	density	3000kg/m^3
nstep	number of timesteps	200
δt	timestep value	20kyr
ncellx	nb of cells in x direction	150
ncelly	nb of cells in y direction	30

3.1 Let's run the code

You will find the *elefant* executable is `/aw/cedric/`. Copy it to your local `/data` folder. Create a folder `model1` and place the executable in it. Then bring your terminal prompt to this location.

Run the code by typing the following command at a terminal prompt

```
./elefant -nstep 20
```

The run should last a few minutes. You will see during this time many lines appear on your screen as the code outputs information pertaining to the calculation for every time step.

3.1.1 Using Paraview

In the terminal type

```
paraview &
```

In `OUTPUT/MARKERS` you will find the Paraview files (markers_xxxxxx.vtu) for the markers. Load them all in Paraview and click on 'Apply'. Your screen should look something like this:

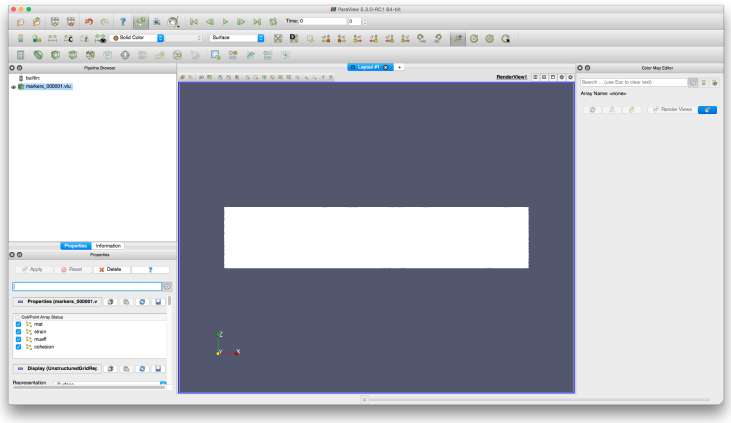

Explore the fields available to you (cohesion $c(\epsilon)$, material id, effective viscosity μ_{eff} and accumulated strain ϵ) as follows:

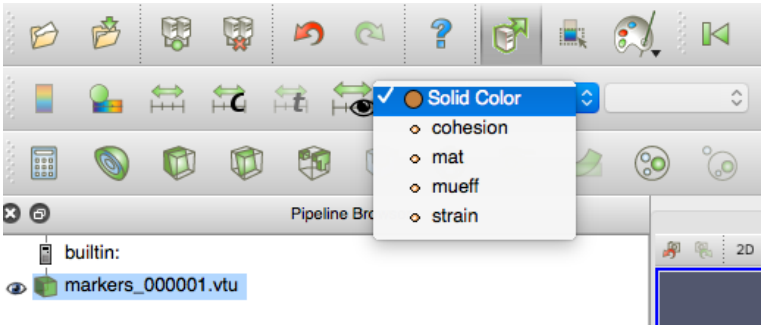

Look at the data over time by clicking on play:

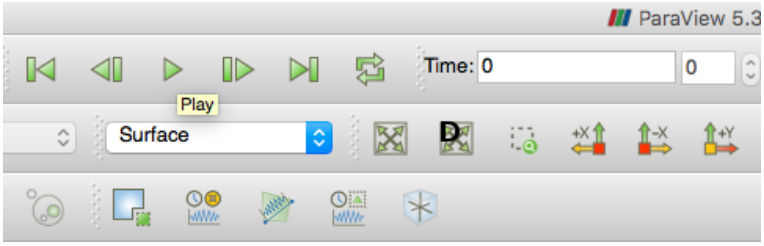

In `/OUTPUT/` you will find the paraview files (*.vtu). Load for instance solution_000010.vtu in paraview. You can visualise the computational grid as follows:

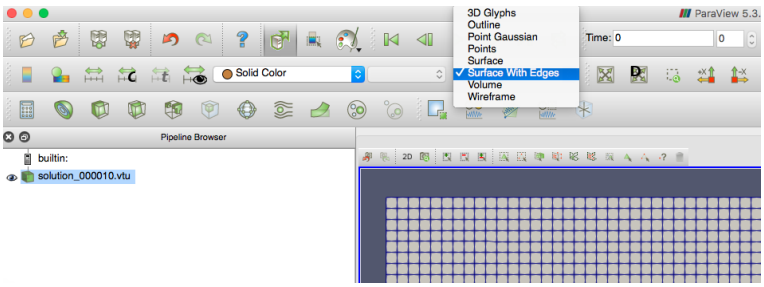

You can/should explore the various fields in the file as follows:

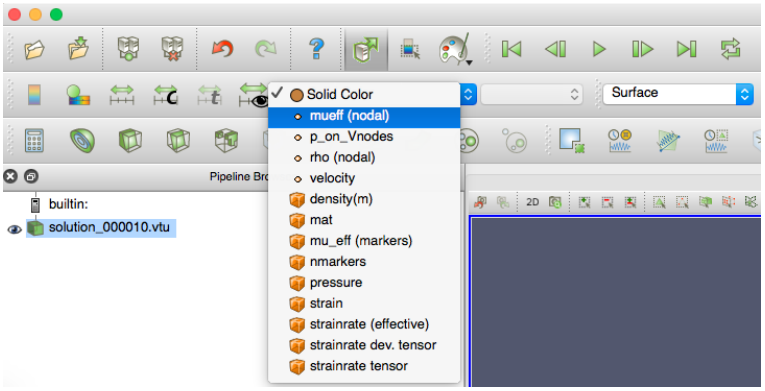

One can also plot the velocity field with arrow glyphs. First click on the glyph icon (top left) then make sure your paraview window looks exactly like the one hereunder:

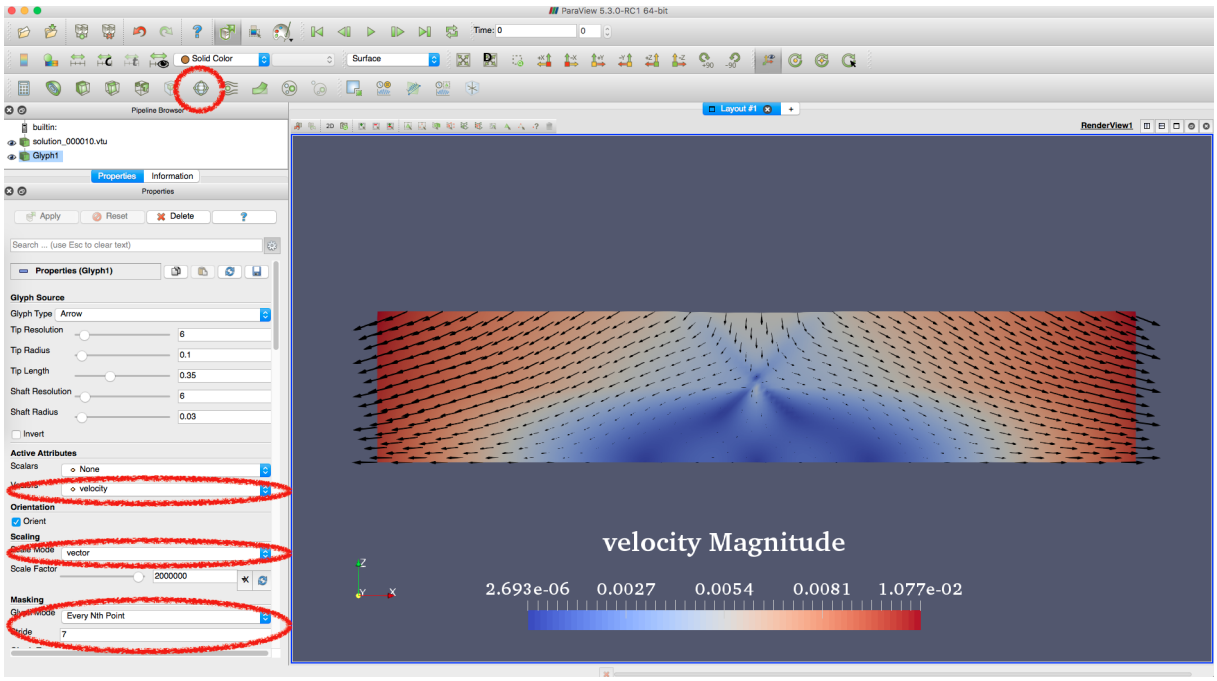

3.1.2 Using gnuplot

Bring the prompt of the terminal to the `OUTPUT/FSURFACE/` folder. You will find in there the free surface topography files *fsurface_xxxxxx.dat*. We will use gnuplot[2] to plot these. In the terminal type:

```
gnuplot
```

At the gnuplot terminal, type

```
plot 'fsurface_000010.dat' w lp
```

and the following window should open on your screen:

[2] http://www.gnuplot.info/

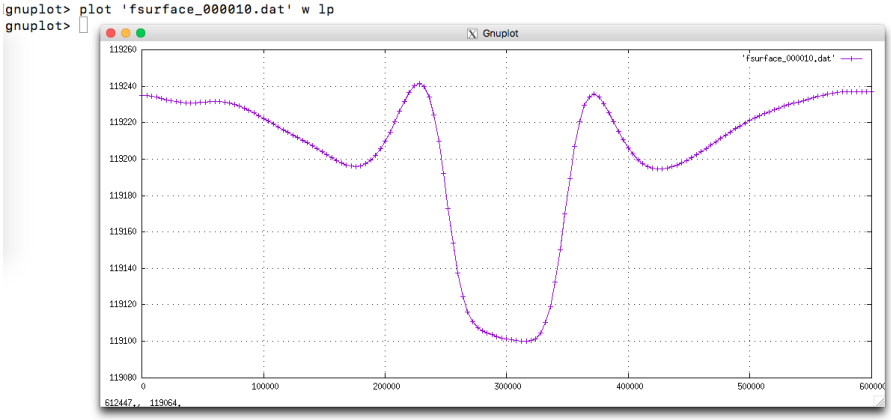

You can visualise multiple files at the same time as follows:

```
plot 'file1.dat' w lp, 'file2.dat' w lp, 'file3.dat' w lp , ...
```

You will find there (http://physics.ucsc.edu/~medling/programming/gnuplot_tutorial_1/index.html) an excellent primer on how to interactively work with gnuplot.

Note that the first column of the free surface files contains the x coordinates of the nodes, the second and third are respectively the x- and y-components of the velocity (in m/s) and the fifth one contains the relative topography (i.e. the topography minus its average).

Scaling the data being visualised can be done as follows:

```
plot 'fsurface_000010.dat' u ($1/1000.):($5/1000.) w lp
```

(In this case it brings both colums from meters to kilometers).

gnuplot can also be scripted. One advantage of such an approach is that gnuplot can then generate a pdf file with the figure you are interested in. You should create a file, say *mygnuplot.script* which contains the following lines:

```
set term pdf enhanced
set grid
set output 'myoutput.pdf'
set xlabel 'x-axis'
set ylabel 'y-axis'
plot 'file.dat' with lp title 'opla'
```

At the prompt of the terminal you can then run gnuplot as follows:

```
gnuplot mygnuplot.script
```

This should have produced the myoutput.pdf file in the same folder.

3.2 Tasks ahead

You will be looking at various models of increasing complexity. These are succinctly described in the following table:

model	lower layer	viscosity	temperature	seed
1	linear	$\mu_0 = 10^{21-22-23}$Pa.s	no	☐
2	linear	$\mu_0 = 10^{21-22-23}$Pa.s	passive	☐
3	linear	$\mu_0 = 10^{21-22-23}$Pa.s	$\rho(T)$	☐
4	nonlinear	Dry Olivine	$\rho(T)$ and $\mu(T)$	☐
5	nonlinear	Wet Olivine	$\rho(T)$ and $\mu(T)$	☐
6	nonlinear	Wet Olivine	$\rho(T)$ and $\mu(T)$	diffuse

3.3 Effect of lower layer viscosity - model1

Following [17] we wish to explore the effect of the lower layer viscosity. You can do so by running the code as follows:

```
./elefant -model 1 -mu0 1.d21
./elefant -model 1 -mu0 1.d22
./elefant -model 1 -mu0 1.d23
```

Run all three models sequentially. Save the data for each and look specifically at (and compare)

- the mode of deformation
- the final topography
- the strainrate field

3.4 A first look at temperature - model2

The previous model was isothermal but this new model is not: the heat transport equation is solved throughout the simulation but temperature is not 'seen': neither the density nor the viscosity depend on it. As such we could call it passive since the velocity obtained by solving the mass and momentum equations is needed to advect it but temperature itself has no influence on those equations.

The temperature is set to 0°C at the surface and at 1330°C at the bottom. A (linear) conductive temperature is prescribed at startup in the whole domain.

Look at the temperature field for all three viscosities of the previous model. Plot isocontours every 100 degrees (Google how to do isocontours with Paraview).

3.5 Temperature-dependent density - model3

In this model, we are now going to couple the density to the temperature field. In first approximation, this dependency takes the form

$$\rho(T) = \rho_0(1 - \alpha(T - T_0))$$

where α is the thermal expansion coefficient, which is typically equal to $3 \times 10^{-5}\mathrm{K}^{-1}$.

Plot and compare the topography at $t = 2M$yr and $t = 4$Myr. Look at the topography difference between model 2 and this one for all three viscosities μ_0.

3.6 Temperature-dependent density and viscosity - model 4,5

The viscosity of the lower layer is now given by a dry/wet olivine dislocation creep rheology [19]:

$$\mu_{ds} = \frac{1}{2} A^{1/n} \dot{\epsilon}^{\frac{1}{n}-1} \exp\left(\frac{Q + pV}{nRT}\right)$$

where A is the prefactor coefficient, n is the nonlinear exponent, Q is the activation energy, V is the activation volume, R is the gas constant and $\dot{\epsilon}$ is the square root of the second invariant of the strainrate tensor.

The values for the dry and wet olivine are shown in the following table [19]:

parameter	dry	wet
A	2.417d-16	3.9063d-15
n	3.5	3
Q	540 kJ	430 kJ
V	20×10^{-6} m^{-3}	15×10^{-6} m^3

All other material properties and parameters are kept identical to the previous experiments.

Run both models

```
./elefant -model 4
./elefant -model 5
```

Look at the topography, style of deformation and viscosity field inside the lower layer. Compare the mode of deformation between both models.

3.7 Temperature-dependent density and viscosity with diffuse seed - model 6

This model is identical to model 5 with the exception of the weak seed. The compact and square one has indeed been replaced by a much wider zone: it is now 100×10km. Also, the seed zone is no more 100% strain weakened put partially strain weakened (it still contains pristine plastic material) in a random manner.

Run this model and explore its mode of deformation.

3.8 Food for thought and bonus questions

depending on how fast you go this week I will flesh out a few of these in the coming days

- what could such a seed be in reality?
- what happens when strainweakening effects are removed?
- Tmoho value at 550 at 30km depth
- introduce crustal layer
- look at xmas tree ? stress crosses ?

References

[1] M. Albertz, C. Beaumont, J.W. Shimeld, S.J. Ingsand, and S. Gradmann. An investigation of salt tectonic structural styles in the Scotian Basin, offshore Atlantic Canada: Part 1, comparison of observations with geometrically simple numerical models. *Tectonics*, 29, 2010.

[2] J. Allen and C. Beaumont. Continental Margin Syn-Rift Salt Tectonics at Intermediate Width Margins. *Basin Research*, page doi: 10.1111/bre.12123, 2014.

[3] V. Allken, R. Huismans, and C. Thieulot. Three dimensional numerical modelling of upper crustal extensional systems. *J. Geophys. Res.*, 116:B10409, 2011.

[4] V. Allken, R. Huismans, and C. Thieulot. Factors controlling the mode of rift interaction in brittle-ductile coupled systems: a 3d numerical study. *Geochem. Geophys. Geosyst.*, 13(5):Q05010, 2012.

[5] V. Allken, R.S. Huismans, H. Fossen, and C. Thieulot. 3D numerical modelling of graben interaction and linkage: a case study of the Canyonlands grabens, Utah. *Basin Research*, 25:1–14, 2013.

[6] J.J. Armitage, T.J. Henstock, T.A. Minshull, and J.R. Hopper. Lithospheric controls on melt production during continental breakup at slow rates of extension: Application to the North Atlantic. *Geochem. Geophys. Geosyst.*, 10(6), 2009.

[7] S. Buiter, A.Y. Babeyko, S. Ellis, T.V. Gerya, B.J.P. Kaus, A. Kellner, G. Schreurs, and Y. Yamada. The numerical sandbox: comparison of model results for a shortening and an extension experiment. *Analogue and Numerical Modelling of Crustal-Scale Processes. Geological Society, London. Special Publications*, 253:29–64, 2006.

[8] S.J.H. Buiter, R.S. Huismans, and C. Beaumont. Dissipation analysis as a guide to mode selection during crustal extension and implications for the styles of sedimentary basins. *J. Geophys. Res.*, 113(B06406), 2008.

[9] E. Burov and A.Poliakov. Erosion and rheology controls on synrift and postrift evolution: Verifying old and new ideas using a fully coupled numerical model. *J. Geophys. Res.*, 106(B8):16,461–16,481, 2001.

[10] G. Corti. Evolution and characteristics of continental rifting: Analog modeling-inspired view and comparison with examples from the East African Rift System. *tectonophyscis*, 522–523:1–33, 2012.

[11] S. Dyksterhuis, P. Rey, R.D. Mueller, and L. Moresi. Effects of initial weakness on rift architecture. *Geological Society, London, Special Publications*, 282:443–455, 2007.

[12] M. Fortin. Old and new finite elements for incompressible flows. *Int. J. Num. Meth. Fluids*, 1:347–364, 1981.

[13] R. Huismans and C. Beaumont. Depth-dependent extension, two-stage breakup and cratonic underplating at rifted margins. *Nature*, 473:74–79, 2011.

[14] R. S. Huismans and C. Beaumont. Symmetric and asymmetric lithospheric extension: Relative effects of frictional-plastic and viscous strain softening. *J. Geophys. Res.*, 108 (B10)(2496):doi:10.1029/2002JB002026, 2003.

[15] R.S. Huismans and C. Beaumont. Roles of lithospheric strain softening and heterogeneity in determining the geometry of rifts and continental margins. In *Imaging, Mapping and Modelling Continental Lithosphere Extension and Breakup*, volume 282, pages 111–138. Geological Society, London, Special Publications, 2007.

[16] R.S. Huismans and C. Beaumont. Complex rifted continental margins explained by dynamical models of depth-dependent lithospheric extension. *Geology*, 36(2):163–166, 2008.

[17] R.S. Huismans, S.J.H. Buiter, and C. Beaumont. Effect of plastic-viscous layering and strain softening on mode selection during lithospheric extension. *J. Geophys. Res.*, 110:B02406, 2005.

[18] L. Jeanniot, N. Kusznir, G. Mohn, G. Manatschal, and L. Cowie. Constraining lithosphere deformation modes during continental breakup for the Iberia–Newfoundland conjugate rifted margins. *tectonophyscis*, 680:28–49, 2016.

[19] S.-I. Karato and P. Wu. Rheology of the Upper Mantle: A synthesis. *Science*, 260:771–778, 1993.

[20] A. Lavecchia, C. Thieulot, F. Beekman, S. Cloetingh, and S. Clark. Lithosphere erosion and continental breakup: Interaction of extension, plume upwelling and melting. *Earth Planet. Sci. Lett.*, 467:89–98, 2017.

[21] J. Liao and T. Gerya. Influence of lithospheric mantle stratification on craton extension: Insight from two-dimensional thermo-mechanical modeling. *Tectonophysics*, page doi:10.1016/j.tecto.2014.01.020, 2014.

[22] G.S. Lister, M.A. Etheridge, and P.A. Symonds. Detachment faulting and the evolution of passive continental margins. *Geology*, 14:246–250, 1986.

[23] D. McKenzie. Some remarks on the development of sedimentary basins. *Earth Planet. Sci. Lett.*, 40:25–32, 1978.

[24] J.B. Naliboff, S.J.H. Buiter, G. Péron-Pinvidic, P.T. Osmundsen, and J. Tetreault. Complex fault interaction controls continental rifting. *Nature Communications*, 8:1179, 2017.

[25] C. Thieulot. FANTOM: two- and three-dimensional numerical modelling of creeping flows for the solution of geological problems. *Phys. Earth. Planet. Inter.*, 188:47–68, 2011.

[26] J.W. van Wijk. Role of weak zone orientation in continental lithosphere extension. *Geophys. Res. Lett.*, 32(L02303), 2005.

[27] J.W. van Wijk and D.K. Blackman. Dynamics of continental rift propagation: the end-member modes. *Earth Planet. Sci. Lett.*, 229:247–258, 2005.

[28] B. Wernicke and B.C. Burchfiel. Modes of extensional tectonics. *Journal of Structural Geology*, 4(2):105–115, 1982.

[29] C. Wijns, R. Weinberg, K. Gessner, and L. Moresi. Mode of crustal extension determined by rheological layering. *Earth Planet. Sci. Lett.*, 236:120–134, 2005.

[30] G. Wu, L.L. Lavier, and E. Choi. Modes of continental extension in a crustal wedge. *Earth Planet. Sci. Lett.*, 421:89–97, 2015.